Rescattering effects in streaking experiments of strong-field ionization

Michał Mandrysz,[1,*] Matthias Kübel,[2,3,4] Jakub Zakrzewski,[1,5] and Jakub S. Prauzner-Bechcicki[1]

[1]*Instytut Fizyki im. Mariana Smoluchowskiego, Uniwersytet Jagielloński, Łojasiewicza 11, 30-348 Kraków, Poland*

[2]*Department of Physics, Ludwig-Maximilians-Universität Munich, D-85748 Garching, Germany*

[3]*Joint Attosecond Science Laboratory, National Research Council and University of Ottawa, 100 Sussex Drive, Ottawa, Ontario K1A 0R6, Canada*

[4]*Institute for Optics and Quantum Electronics, University of Jena, D-07743 Jena, Germany*

[5]*Mark Kac Complex Systems Research Centre, Jagiellonian University, Łojasiewicza 11, 30-348 Kraków, Poland*

(Received 12 July 2019; published 6 December 2019)

Strong-field ionization provides unique means to address complex dynamics of an electron in competing Coulomb and laser fields. A recent streak camera experiment [M. Kübel *et al.*, Phys. Rev. Lett. **119**, 183201 (2017).] analyzed asymmetries in the low-energy region of ejected electron momentum distributions and associated them with multiple rescattering of the electron on the parent ion. In this work we directly confirm the multiple-rescattering nature of the asymmetry in the low-energy region. Such electron-ion collisions cannot be described within one-dimensional simulations even taking into account focal-volume averaging. Using a time-dependent Schrödinger equation simulation in two dimensions supplemented by insights from the strong-field semiclassical approximation we identify the dominant interference features of the complex photoelectron momentum distributions and find their traces in the experiment. In particular, the holographic structures remain visible in experimental results averaged over the carrier-envelope phase (CEP). In the case of individual momentum distributions when the CEP or delay between the two pulses is varied, the structures arising due to rescattering events are influenced by interfering electrons ionized at the main peaks of the electric field. With an increase of experimental resolution, such structures record the electron dynamics on a sub-laser-cycle timescale.

DOI: 10.1103/PhysRevA.100.063410

I. INTRODUCTION

The interaction of atoms and molecules with intense, very short laser pulses results in many interesting phenomena, such as high-order harmonic generation, above-threshold ionization (ATI), or nonsequential multiple ionization. All these phenomena have been studied carefully since the 1980s with the use of both theoretical and experimental tools [1–3]. The experiments are becoming more and more refined, even allowing one to resolve dynamics of electron wave packets at the attosecond timescale [4,5]. Such a situation sets high the bar for the theory. Theoretical description in many cases requires a nonperturbative treatment and, eventually, ends with simplified modeling and computer simulations [6]. This happens because, despite an enormous increase in available computer resources, full *ab initio* quantum calculations of processes involving more than one electron are typically beyond reach.

In view of the above, the single active electron (SAE) approximation appears as a very powerful tool. In fact, one may relatively easily solve a full three-dimensional (3D) time-dependent Schrödinger equation (TDSE) for an atom with a single electron exposed to an external field with a given set of parameters [7] without the necessity of referring to restricted geometry models [6]. Importantly, the external field may have parameters, i.e., amplitude, frequency, envelope, carrier-envelope phase (CEP), and often duration, in ranges that are used in experiments. Already for two-electron atoms similar calculations are very demanding with respect to computer resources. To the best of our knowledge this has been done only for helium [5,8–13]. The proper comparison of numerical results from such full 3D calculations with experimental data imposes the usage of various averaging techniques like focal-volume or the Gouy-phase averaging [14]. The averaging, in turn, calls for large data sets covering specific ranges of parameters resulting, in the course of time, in excessive computational demands. Thus, a judiciously chosen restricted geometry model may be a good trade-off offering better agreement with experimental data at less expense and granting enhanced insight. Indeed, numerical solutions of the TDSE in various simplified models lead to results closely resembling experimental data especially for some quantities of interest, such as dipole acceleration [15].

In general, the interpretation of TDSE results requires the use of certain analytic methods such as the strong-field approximation (SFA) [16–18]. When applied to photoelectron momentum distributions it becomes possible to separate the individual processes and trajectories that correspond to them. These trajectories interfere with each other and, ultimately, lead to a very complex final image. The reasoning can also be applied in reverse: the image encodes the dynamics dictated by the Hamiltonian and thus photoelectron spectroscopy can be done by the analysis of the image.

*michal.mandrysz@student.uj.edu.pl

Recently, Kübel *et al.* [4] demonstrated a streak camera that allows one to temporally resolve strong-field ionization induced by linearly polarized short pulses. They called their method subcycle tracing of ionization enabled by infrared (STIER). The setup used in the experiment is a kind of pump-and-probe one, i.e., a few-cycle, intense, linearly polarized pulse in the near-visible spectral range (VIS pulse) induces ionization, whereas a moderately intense, mid-infrared pulse (IR pulse) streaks photoelectrons allowing observation of subcycle dynamics of strong-field ionization. In particular, Kübel *et al.* observed an asymmetry in the yield of low-energy electrons associated with the rescattering process. Interestingly, the respective asymmetry in the yield has not been fully reproduced by the authors through solving a one-dimensional (1D) TDSE, in spite of taking into account both the focal-volume averaging (FVA) and integration over the Gouy phase. The discrepancy between experimental and computational results is ascribed to the observation that the 1D model cannot capture the details of the recollision processes accurately. Thus, the part of yield related to recolliding electrons is poorly modeled.

The main aim of this work is to provide a more realistic simulation of the experiment. This allows us to understand the limitations of the 1D description. More importantly, supplementing the numerics with SFA insight we identify the main interference features present in momentum spectra. We solve the 2D TDSE within the SAE approximation and collect data sets of intensities, phases, and delays significant enough to allow for the focal-volume averaging and the integration over the Gouy phase in a manner similar to that in [4]. We present calculated 2D momentum distributions and directly compare them to previously unpublished experimental data. The obtained 2D momentum distributions display complex features which we also analyze within the SFA framework. Our results reveal a complex ring structure that arises from the interference of attosecond wave packets produced at different half-cycle maxima. The role of multiple electron rescattering in the formation of the asymmetry feature described in Ref. [4] is confirmed.

II. METHODS

A. TDSE simulation

The main part of the calculations concerned with momentum distributions followed closely the method outlined in [4], but with an increased dimensionality. Momentum distributions were found using 1D and 2D TDSE simulation performed in Cartesian coordinates. A reasonable doubt can be cast as to whether the results using a full 3D dynamics with the help of spherical harmonics would not differ substantially, due to, e.g., the glory phenomenon [19]. Our experience with a limited range of 3D simulations for this particular setup allows us to say that the difference is practically negligible. Calculations are performed in the length gauge and assume a simplified description of the external field (see Fig. 1). The TDSE solver is based on the split operator method and the fast Fourier transformation algorithm as implemented in software developed by us for other restricted dimensionality models [6,20–22]. The values of parameters used were $dt = 0.05$ (evolution time step), $dx = \frac{100}{512} \approx 0.2$ (grid spacing), and $N = 28\,672$ (number of grid point in one direction). The ground state was found using propagation in imaginary time. Both pulses were linearly polarized with respect to the z axis and the respective wavelengths and peak intensities were ($\lambda_{\mathrm{VIS}} = 735$ nm, $I_{\mathrm{VIS}} = 7 \times 10^{14}$ W cm^{-2}) and ($\lambda_{\mathrm{IR}} = 2215$ nm, $I_{\mathrm{IR}} = 3 \times 10^{13}$ W cm^{-2}). The pulse shape is identical to the one from the original paper of Kübel *et al.* [4]; namely, the IR pulse is approximated by a cos wave, with a significantly shorter duration (as compared with experiment) of 4.25 cycles of length $\tau_{\mathrm{IR}} \approx 7.4$ fs each and 0 field strength at the beginning. The envelope for the VIS pulse has a full width at half maximum (FWHM) of 5 fs (see Fig. 1):

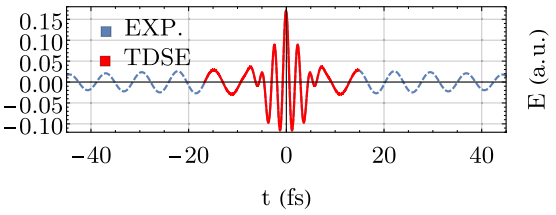

FIG. 1. Exemplary two-color field used for the simulations [red line, corresponding to $\phi = 0$, $\tau = 0(\tau_{\mathrm{IR}})$], compared with field used in the experiment (dashed blue). The rising and falling tails are cropped from this picture.

$$\boldsymbol{E}(t) = E_{\mathrm{VIS}}(t)\boldsymbol{e}_z + E_{\mathrm{IR}}(t)\boldsymbol{e}_z, \tag{1}$$

where

$$E_{\mathrm{VIS}}(t) = F_{\mathrm{VIS}} f(t-\tau)\cos[\omega_{\mathrm{VIS}}(t-\tau)+\phi], \tag{2}$$

$$E_{\mathrm{IR}}(t) = F_{\mathrm{IR}}\cos(\omega_{\mathrm{IR}} t). \tag{3}$$

Here F_i and ω_i stand for field amplitude and frequency of the corresponding pulse, respectively, $f(t-\tau)$ is a Gaussian envelope of the VIS pulse, τ is the delay between pulses, and ϕ is the CEP of the VIS pulse (in the later part of this article we will use the symbol ϕ and CEP interchangeably).

B. Postprocessing and fitting data to experiment

The well-known affliction of laboratory strong-field experiments is the inherent spatial averaging due to nonuniformity of laser beam cross section and geometry of the optical elements.

The most straightforward recipe for adapting theoretical calculations is to average over intensities with the weight of inverse intensity [23], in other words, calculating the integral

$$\int_0^{I_0} dI\, P(I)/I. \tag{4}$$

Such a method will be referred to as a focal-volume average (FVA). On the other hand, more advanced measures could be employed taking into account the Gouy phase [24]. Surprisingly, in our case these averaging methods did not lead to an improvement over the nonaveraged (single intensity) results; to the contrary, their application (especially accounting for the Gouy phase) caused an underestimation in the width of momentum spectra when a single delay was considered. This can be understood as follows. The action of FVA can be reduced to mixing the thin (in terms of width), low-intensity

momentum distributions with the wide, high-intensity momentum distributions. Since the former usually obtain much higher weights, the averaged distribution appears thinner than the original one. On the other side, in the experiment, the synchronization jitter between IR and VIS pulses and the focal geometry can effectively lead to uncertainties in the time delay, the effect which broadens the distributions. Moreover, FVA becomes harder to implement correctly when two-color pulses are considered. Consequently, we have restricted our analysis to the simple volume average given by Eq. (4) (FVA), the delay (±0.8 fs) average (DA), or combining the two into the delay and focal volume average (DFVA). After averaging, the obtained momentum distributions were smoothed using a median filter [25] and (point) resampled to the (smaller) resolution of experimental results. Since the experiment provided data over a wide range of delays but the absolute information about the CEP [ϕ in Eq. (2)] was not determined completely, the CEP dependence of the TDSE and experimental results had to be compared and matched. To aid our analysis we have employed a secondary measure of (dis)similarity, based on the least-squares method applied to momentum distributions obtained from the experiment and simulation (where the simulation data have been normalized and gently smoothed out to match the experimental resolution), parametrized by the CEP shift and experimental delay. This automated method yielded the CEP shift and the experimental delay $0(\tau_{\mathrm{IR}})$ (corresponding to the center of the VIS pulse centered at a maximum of the IR field, see Fig. 1, also delay ≈5.87 fs from [4]), as the most consistent with our 2D results [Fig. 2(b)] for raw data and DFVA data. In the case of 1D results [Fig. 2(a)], the raw CEP spectrum matched the delay $-2(\tau_{\mathrm{IR}})$ (separated by 2 τ_{IR} from the correct 2D match) which is unexpected yet acceptable, because the IR field strength decreased slightly in the experiment when moving away from delay $0(\tau_{\mathrm{IR}})$. However the DFVA matched with the opposite side of the momentum axis which is incorrect. This result suggests that the automated matching techniques of experimental data to low-dimensional models, especially ones involving averaging techniques, can be deceitful, and some additional information is needed for a successful match. Nevertheless, such problems become absent in the case of higher-dimensional models as Fig. 2(b) suggests.

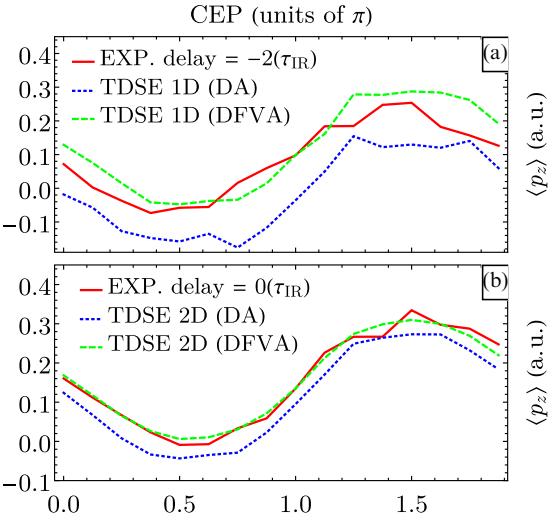

FIG. 2. The experimental CEP dependence of the mean momentum in the z direction, $\langle p_z \rangle$, is compared to the results of 1D (a) and 2D (b) simulations. Note that the best fits between experiment and 1D or 2D calculations, respectively, are obtained for delay values, which differ by 2 IR periods (see text for details).

III. RESULTS

A. Comparison with experiment: 1D and 2D simulations

The momentum distributions obtained from the 1D and 2D TDSE at $\tau = 0(\tau_{\mathrm{IR}})$ are compared with experimental data at two different CEP values in Fig. 3. To facilitate the comparison, in the 2D case the results were projected on the axis parallel to the polarization axis. We notice (compare also with Fig. 4(c) of [4]) a quite good overall agreement of 1D simulations with experimental curves; still 2D results are clearly superior reproducing the experiment in quite a remarkable way. One may also observe that combining the delay and focal average (DFVA) leads to subtle and important changes in the momentum distributions, such as smoothing out a prominent peak appearing in DA data at $p_z \simeq 1.2$ for CEP = 0, leading to better agreement with the experimental data. This shows that some features of momentum distributions will remain undetectable in the experiment, due to fundamental limitations connected to laser pulse nonuniformity.

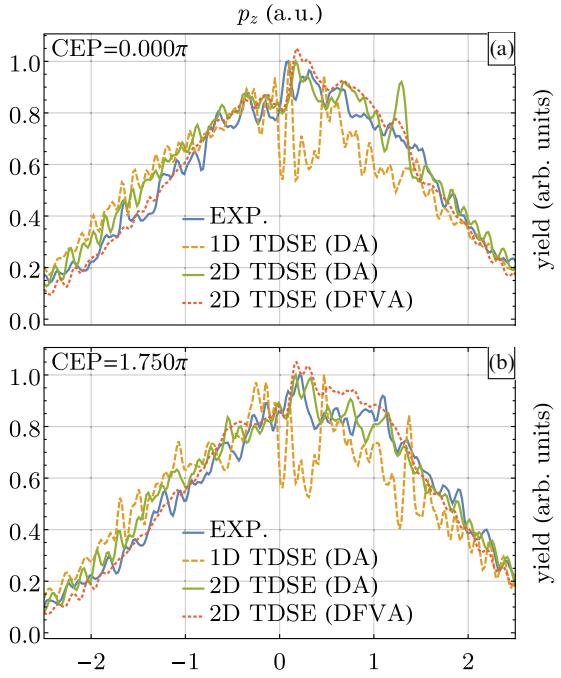

FIG. 3. Comparison of momentum distributions for $\tau = 0(\tau_{\mathrm{IR}})$, at different CEP values indicated in the figure for experimental data [blue (gray), solid], nearby-delay averaged (DA) 1D simulations (yellow), 2D simulations [green (light gray), solid], and 2D simulation with a focal-volume and delay (±0.8 fs) averaging (DFVA). The experimental data CEP = 0 were previously published in Fig. 4(c) of [4]; nuance differences come from improved fit over experimental delay for the whole width of the distribution. Notice how the peak [panel (a), $p_z \simeq 1.2$] of 2D TDSE (DA) is washed out by the DFVA.

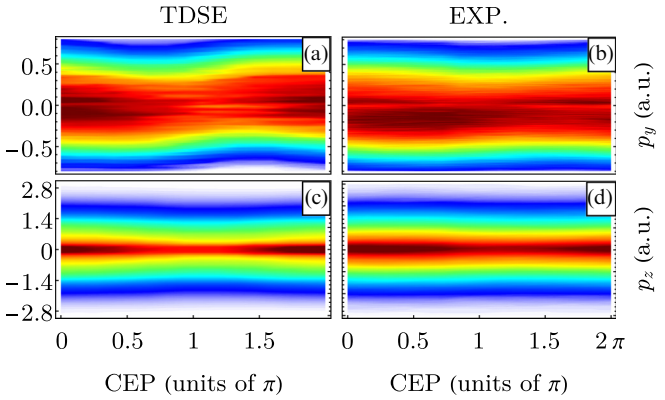

FIG. 4. CEP-dependent momentum distributions at delay $\tau = 0(\tau_{IR})$, in the direction perpendicular to the polarization axis [(a), (b)], and parallel to it [(c), (d)]. The numerical [(a), (c)] and experimental [(b), (d)] data were integrated over delay range of ±0.8 fs.

The agreement of our 2D simulations with experiment may be further verified by side-by-side inspection of DA momentum distributions projected on directions parallel and perpendicular to the polarization axis; see Fig 4. While clearly some small differences are visible the overall agreement is quite satisfactory. The remaining discrepancies may be attributed to low experimental resolution leading to significant uncertainties in fitting parameters and a limited number (three) of averaged delays.

It is insightful to compare CEP-averaged photoelectron momentum distributions predicted by theory [panel (a)] versus experiment [panel (b)] as presented in Fig. 5. Apart from a good agreement between the two results (the theoretical prediction has been smoothed out to aid the comparison), we observe a large asymmetry along the p_z axis. The upper side ($p_z > 0$) is much narrower in p_y than the lower side and exhibits the asymmetric feature at $p_z = 0.2$ a.u., which emerges due to multiple electron rescattering events and Coulombic interaction [4]. This structure is much more pronounced in the simulations.

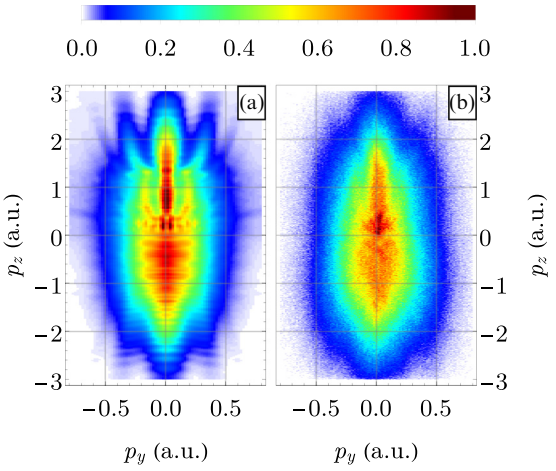

FIG. 5. CEP-averaged 2D photoelectron momentum distributions for $\tau = 0(\tau_{IR})$ parallel (p_z) and perpendicular (p_y) to the laser polarization direction. The TDSE results (a) have been smoothed to mimic the the momentum resolution in the experimental data (b). Traces of the side lobes visible in (a) for $p_z > 0$ are noticeable in (b).

In order to directly test whether the feature at $p_z = 0.2$ a.u. originates in multiple rescattering, in Fig. 6 we present the snapshots of photoelectron momentum distributions (for fixed CEP and delay value) at time instances separated by integer numbers of IR periods (corresponding to zeros of vector potential [26]). The overall structures remain almost stationary after the high-intensity VIS pulse is over [see times $t > 1(\tau_{IR})$ in Fig. 6], with the exception of low-momentum regions for which (for convenience) we provide zoomed windows. Indeed, one can observe the formation of a holographic [27], shell-like structure concentrated around $p_z = 0.2$. The asymmetry builds up with each IR period through simultaneous horizontal (p_y) splitting and shifting toward lower p_z values. This nonequilibrium steady structure emerges through interference of both forward and backward rescattered electrons accelerated by the IR field [18,28]. Comparing time $t = 1(\tau_{IR})$ of Fig. 6 with times $t > 1(\tau_{IR})$ we see a significant increase in phase accumulation in the radial direction from the ($p_y = 0$, $p_z = 0.2$), leading to sharp drops in intensity visible in the zoomed regions, the effect again attributable to multiple rescatterings. The significance of this asymmetry is expected to grow with the wavelength of the IR field [28].

Returning to Fig. 5, at $p_z > 0$ and around $p_y = \pm 0.2$ a.u. in both experiment and simulation, one can notice sidebands parallel to the polarization axis, also known as holographic structures [27]. The feature is visibly less pronounced in the experiment than in the simulation due to limited resolution (high-resolution experiments using the STIER technique are currently in preparation). In general holographic structures can be attributed to interference of two coherent wave packets ionized at two nearby (same quarter-cycle) instances of time. One of such wave packets (signal) is assumed to rescatter with the parent ion before meeting the other (reference) wave packet. These kinds of processes occur frequently in this setup as can be seen on the positive part of the p_z axis in Fig. 7(a), which presents photoelectron momentum distributions as a function of VIS field CEP (ϕ) value. The frequent occurrence of rescattering events is also the reason why such side lobes are visible on CEP-averaged plots such as Fig. 5.

The holographic structures seen on detailed distributions in Fig. 7(a) are also heavily influenced by other subcycle effects, including interference of wave packets ionized with half, one, or more cycle delays. One of the most dominant traces of these effects is the ring structure centered at $p_z = 0$ for CEP $= \pi$ and of approximately 0.25 a.u. (first) radius [compare Fig. 7(a), third panel from the left]. This ring structure is displaced along the p_z axis with the change of CEP value [see Fig. 7(a)]. In experiments using the RABBITT technique similar ring structures have been observed [29,30]. Their displacement from $p_z = 0$ was shown to be proportional to the area under the vector potential between two dominant ionization times in some simpler models. Arguably the present situation is considerably more complex than the setups occurring in the literature. In particular, the vector potential is the sum of IR and VIS contributions, i.e., $\boldsymbol{A}(t) = \boldsymbol{A}_{IR}(t) + \boldsymbol{A}_{VIS}(t)$, and therefore does not behave like a simple sinelike function. Nevertheless, given the versatility of the SFA [17] we suspect that a similar analysis might be valuable. Thus, resorting to SFA analysis below we show that the CEP displacement of the ring is in fact due to interference resulting

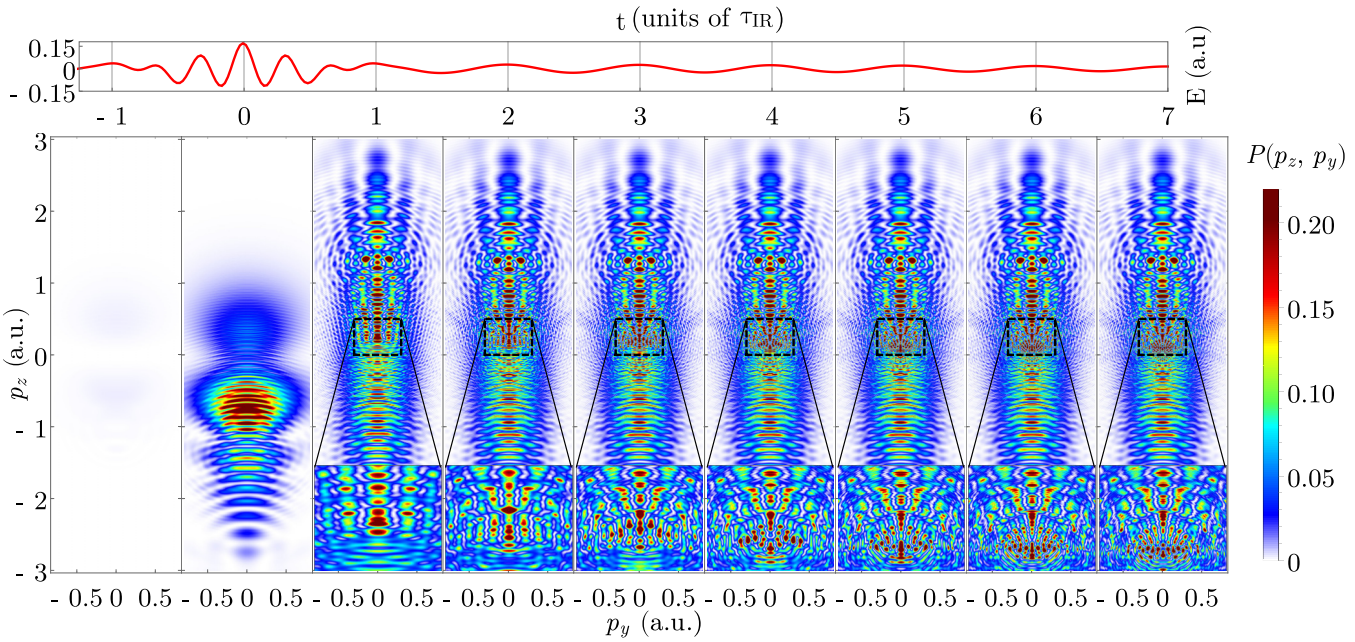

FIG. 6. Momentum distributions snapshots at equal IR period intervals for exemplary delay $= -1(\tau_{\mathrm{IR}})$, CEP $= 0$. The overall distribution is stable after the second cycle (τ_{IR}). Significant changes appear for several optical cycles in the low-momentum areas [zoom on the area $p_z = (0, 0.5)$, $p_y = (-0.3, 0.3)$ is presented in each snapshot].

from a few (2 or 3) dominant ionization times (see Fig. 8) and only weakly dependent on the $\boldsymbol{A}_{\mathrm{VIS}}(t)$ contribution.

B. SFA analysis

Since the SFA is a well-known method (see [17] for a review) we describe it only briefly. The ionization amplitude a_p and action $S(t)$ are given by

$$a_p = -i \int_{-\infty}^{\infty} \boldsymbol{E}(t') \cdot \boldsymbol{d}(\boldsymbol{p} + \boldsymbol{A}(t')) e^{-iS(t')} dt', \tag{5}$$

$$S(t) = \int_{t}^{\infty} \left[\frac{[\boldsymbol{p} + \boldsymbol{A}(t')]^2}{2} + I_p \right] dt', \tag{6}$$

$$\boldsymbol{d}(\boldsymbol{p}) = \frac{\boldsymbol{p}}{(\boldsymbol{p}^2 + 2I_p)^3}, \tag{7}$$

where I_p is the ionization potential. Assuming that the ionization takes place at the extrema of the total electric field, which in our case can be approximated with the extrema of the VIS field, we get

$$t_n = \left(n - \frac{\phi}{\pi} \right) \tau_{\mathrm{VIS}}/2, \tag{8}$$

for most likely times t_n of ionization. Then Eqs. (5) and (6) can be reduced to

$$a_p = \sum_n E_z(t_n) d_z(\boldsymbol{p} - \boldsymbol{A}(t_n)) e^{-iS(t_n)}, \tag{9}$$

$$S(t_n) = -\left(\frac{\boldsymbol{p}^2}{2} + I_p \right) t_n - p_z \int_0^{t_n} \left[A(t') + \frac{A(t')^2}{2} \right] dt'. \tag{10}$$

The resulting probability $|a_p|^2$ is presented as a function of CEP in Fig. 7(b) and 7(c). For the sake of clarity, above each momentum distribution we present a diagram showing the VIS + IR laser field (green lines) and the IR vector potential in the background (red lines). Blue dashed lines point to ionization times, Eq. (8), taken into account in the analysis. First, we take into account two ionization times $\{t_0, t_2\}$ [Fig. 7(b)] for which the field points in the same direction. At CEP $=$ 0 one can notice the ring structure centered at just above $p_z = 1$, which intensifies while moving down toward lower p_z values with the increasing value of CEP. For CEP $= \pi$ the contributions from ionization times $\{t_0, t_2\}$ become equal (see Fig. 8) leading to a pronounced ring, centered at $p_z = 0$ with the first radius of approximately 0.25 a.u., in agreement with TDSE results. The rings are preserved even when the IR vector potential alone is considered [$\boldsymbol{A}_{\mathrm{VIS}}(t)$ neglected] in calculating a_p with the help of Eqs. (9) and (10) (result not shown). Moreover, the contribution of the term $A(t')^2/2$ has a small influence on the ring shape and can be dropped in the Eq. (10). Thus, for the readability of the panels in Fig. 7(b) and 7(c), only A_{IR} is shown for reference (red lines).

In Fig. 7(c) we expand the analysis to the case of three ionization times, $\{t_0, t_1, t_2\}$. The interference structures become richer and the ring acquires slight deformations. The addition of more ionization times does not provide more clarity to the overall picture. Other effects, such as multiple rescatterings with the parent ion, provide additional structures which suppress or enhance the visibility of the ring and its surrounding features.

In the case of the changing delay instead of the CEP value, Eq. (8) changes to

$$t_n = n\tau_{\mathrm{VIS}}/2 + \tau, \tag{11}$$

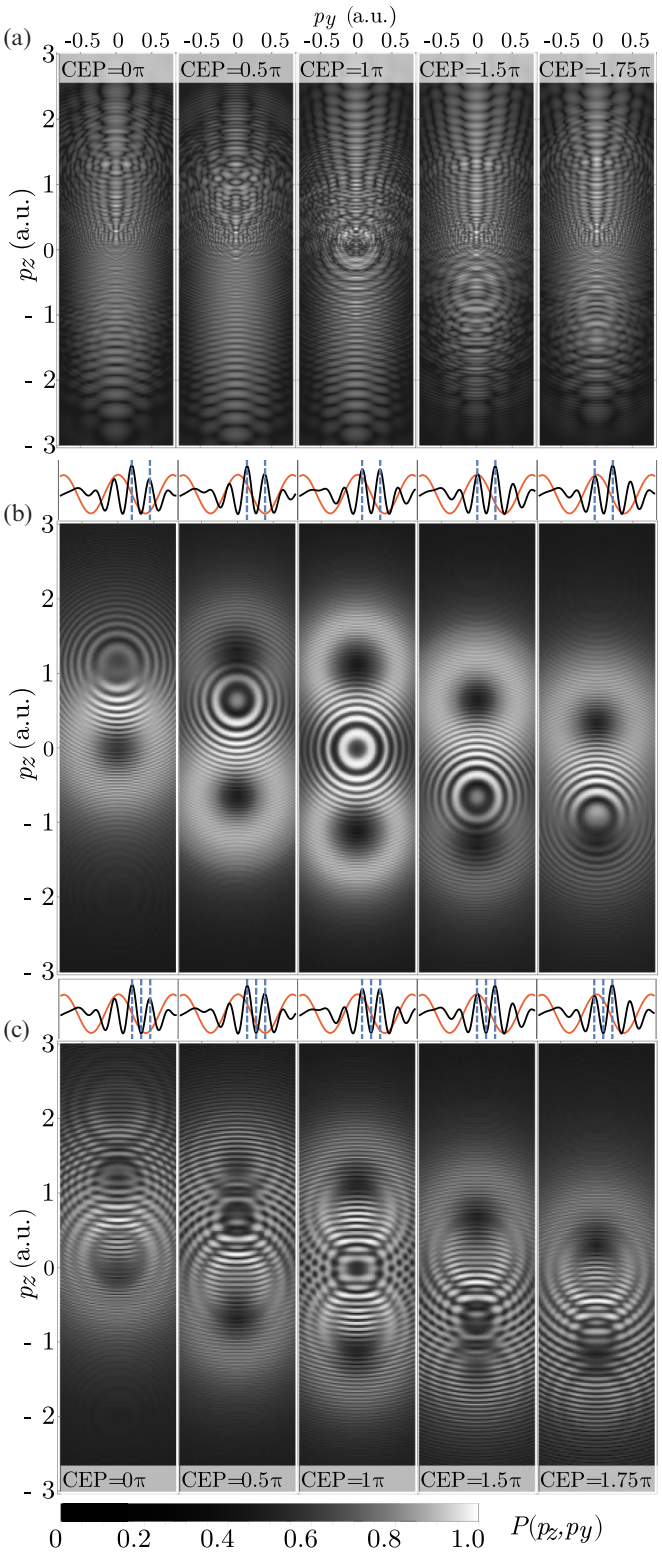

FIG. 7. Momentum distributions for individual CEP values at delay $\tau = 0(\tau_{IR})$. (a) TDSE result, (b) SFA prediction taking into account two ionization times $\{t_0, t_2\}$, (c) same as (b) but considering three ionization times, $\{t_0, t_1, t_2\}$ (details in text). The diagrams on top of panels in (b) and (c) present IR vector potential (red solid line), total electric field (black solid line), and ionization times (dashed blue lines). The position of the ring is correctly described by two dominant peaks, but its shape can be modulated by the third peak.

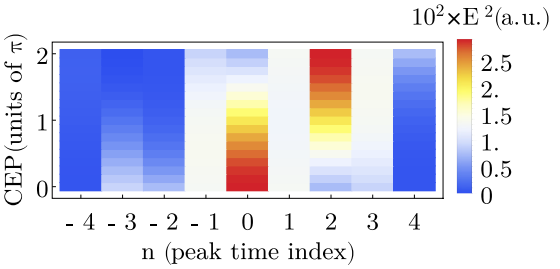

FIG. 8. Field intensity at ionization times t_n for different CEP values and $\tau = 0(\tau_{IR})$. The dominant peaks throughout the whole CEP domain are $\{t_0, t_2, t_1\}$.

while Eqs. (9) and (10) remain valid. Now, in contrast with the varying CEP case (see Fig. 9 and compare it with Fig. 8) it is not trivial to select the ionization peaks contributing the most to the momentum distributions pictured in Fig. 10(a). In fact, many such choices exist. Here we limit our analysis to ionization peaks for which the electric field intensity passes a chosen threshold $[|E(t_n)|^2 > 0.009$ a.u.] and present the results in Fig. 10(b). The abundance of ringlike features could be discouraging at first, but through careful inspection one can see that the vast majority of the ringlike structures of Fig. 10(b) either can be found directly (as rings) or appear to steer the holographic structures found in the TDSE result [Fig. 10(a)]. Although our analysis is by no means exhaustive, we have shown how to understand and interpret one layer of complexity of the TDSE result and how other interference structures can be affected.

IV. DISCUSSION AND SUMMARY

We have shown that 2D TDSE simulations yield substantially better agreement with the experimental results than 1D models. However, fits of computational results to experimental data require some caution, especially when comparing reduced-dimensionality models to experimental data. Averaging over focal volume and Gouy phase needs to be done on par with averaging over "nearby" delays in order to retain the width of the momentum distributions. On the other hand, the individual 2D momentum distributions could not be directly compared due to the limited resolution of the experimental results. Using the CEP-averaged results we have obtained a good agreement between the theory and the experiment. Asymmetric features present in the experimental results have

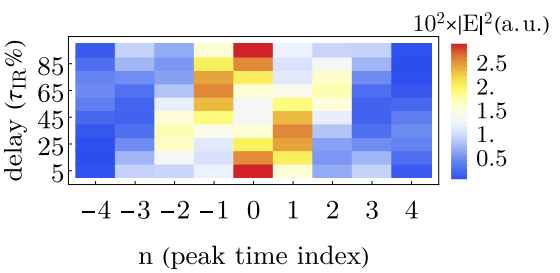

FIG. 9. Field intensity at ionization times t_n for different delay values and CEP = 0. The set of dominant peaks varies with the delay, leading to less straightforward analysis.

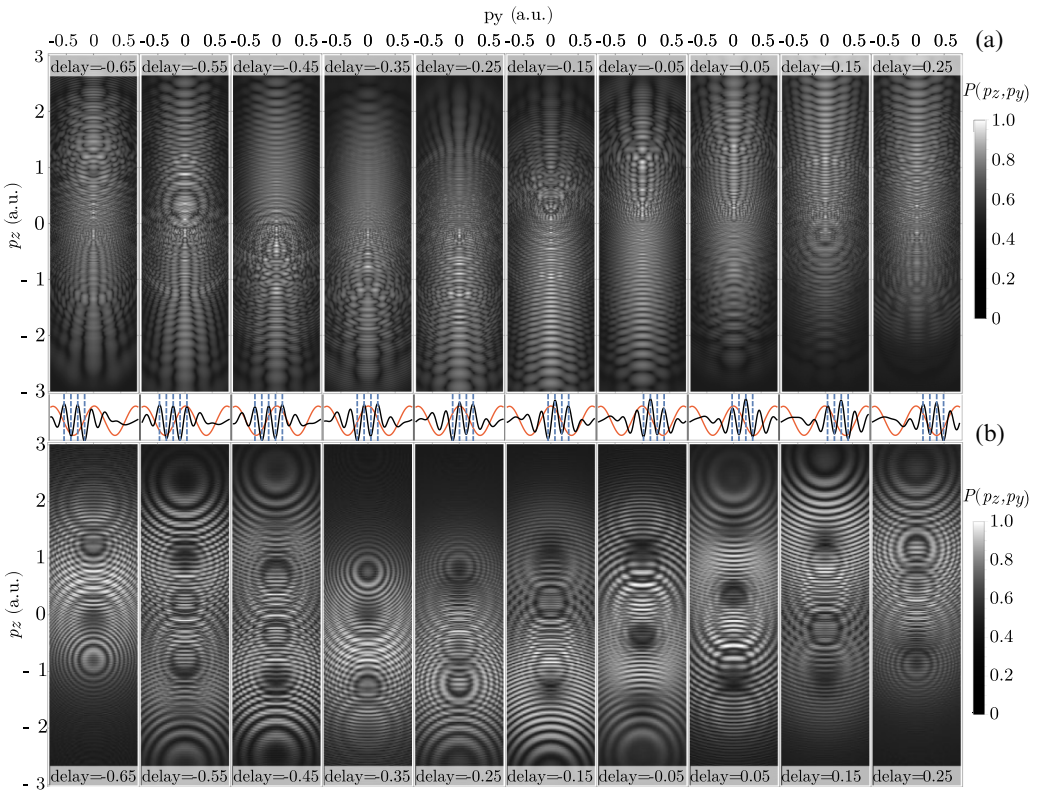

FIG. 10. Photoelectron momentum distributions for individual delays in the units of τ_{IR} and CEP = 0. (a) TDSE result, (b) SFA prediction for ionization times at which electric field surpasses a given threshold (see text). The diagram between panels shows the time dependence of IR vector potential (red solid line), total electric field (black solid line), and ionization times (dashed blue lines). Some of the SFA-predicted rings remain visible in the TDSE result.

been traced to multiple-rescattering effects in the IR field, visible and similar at all CEP values. The complex individual momentum distributions consist of two kinds of structures: holographic lobes extending in the direction perpendicular to the polarization direction, and ATI structures (affecting the holographies) and/or ring structures. In particular, an intense ring centered at CEP $= \pi$ and traversing through the p_z axis with the change of CEP value has been noted. With the use of the SFA we have shown that this ring originates from the interference of two or more wave packets born at different ionization times. In a bit less straightforward way this effect can also be seen when delay instead of CEP is manipulated. Together with the holography, the ring structures record the electron dynamics on a sub-laser-cycle timescale that lead to applications in next-generation photoelectron spectroscopy. Complementary analysis from the perspective of high harmonic generation in the given setup is currently underway.

ACKNOWLEDGMENTS

This project has received funding from the EU's Horizon 2020 research and innovation program under Marie Sklodowska-Curie Grant Agreement No. 657544 (M.K.) and from the National Science Centre, Poland, via Symfonia Project No. 2016/20/W/ST4/00314 (M.M., J.P.B., and J.Z.). We also acknowledge the support of PL-Grid Infrastructure.

[1] W. Becker, X. J. Liu, P. J. Ho, and J. H. Eberly, Rev. Mod. Phys. **84**, 1011 (2012).
[2] P. Agostini and L. F. DiMauro, Rep. Prog. Phys. **67**, 813 (2004).
[3] F. Krausz and M. Ivanov, Rev. Mod. Phys. **81**, 163 (2009).
[4] M. Kübel, Z. Dube, A. Y. Naumov, M. Spanner, G. G. Paulus, M. F. Kling, D. M. Villeneuve, P. B. Corkum, and A. Staudte, Phys. Rev. Lett. **119**, 183201 (2017).
[5] M. Ossiander, F. Siegrist, V. Shirvanyan, R. Pazourek, A. Sommer, T. Latka, A. Guggenmos, S. Nagele, J. Feist, J. Burgdörfer, R. Kienberger, and M. Schultze, Nat. Phys. **13**, 280 (2017).
[6] D. K. Efimov, A. Maksymov, J. S. Prauzner-Bechcicki, J. H. Thiede, B. Eckhardt, A. Chacon, M. Lewenstein, and J. Zakrzewski, Phys. Rev. A **98**, 013405 (2018).
[7] V. Mosert and D. Bauer, Comput. Phys. Commun. **207**, 452 (2016).
[8] D. Dundas, K. T. Taylor, J. S. Parker, and E. S. Smyth, J. Phys. B: At., Mol. Opt. Phys. **32**, L231 (1999).
[9] K. Taylor, J. Parker, K. Meharg, and D. Dundas, Eur. Phys. J. D **26**, 67 (2003).
[10] J. S. Parker, L. R. Moore, D. Dundas, and K. T. Taylor, J. Phys. B: At., Mol. Opt. Phys. **33**, L691 (2000).

[11] A. Emmanouilidou, J. S. Parker, L. R. Moore, and K. T. Taylor, New J. Phys. **13**, 043001 (2011).
[12] J. Feist, S. Nagele, R. Pazourek, E. Persson, B. I. Schneider, L. A. Collins, and J. Burgdörfer, Phys. Rev. A **77**, 043420 (2008).
[13] R. Pazourek, J. Feist, S. Nagele, and J. Burgdörfer, Phys. Rev. Lett. **108**, 163001 (2012).
[14] D. Hoff, M. Krüger, L. Maisenbacher, A. M. Sayler, G. G. Paulus, and P. Hommelhoff, Nat. Phys. **13**, 947 (2017).
[15] M. F. Ciappina, J. Biegert, R. Quidant, and M. Lewenstein, Phys. Rev. A **85**, 033828 (2012).
[16] M. Lewenstein, P. Balcou, M. Y. Ivanov, A. L'Huillier, and P. B. Corkum, Phys. Rev. A **49**, 2117 (1994).
[17] K. Amini, J. Biegert, F. Calegari, A. Chacón, M. F. Ciappina, A. Dauphin, D. K. Efimov, C. Figueira de Morisson Faria, K. Giergiel, P. Gniewek, A. S. Landsman, M. Lesiuk, M. Mandrysz, A. S. Maxwell, R. Moszyński, L. Ortmann, J. Antonio Pérez-Hernández, A. Picón, E. Pisanty, J. Prauzner-Bechcicki, K. Sacha, N. Suárez, A. Zaïr, J. Zakrzewski, and M. Lewenstein, Rep. Prog. Phys. **82**, 116001 (2019).
[18] L.-Y. Peng, W.-C. Jiang, J.-W. Geng, W.-H. Xiong, and Q. Gong, Phys. Rep. **575**, 1 (2015).
[19] Q. Z. Xia, J. F. Tao, J. Cai, L. B. Fu, and J. Liu, Phys. Rev. Lett. **121**, 143201 (2018).
[20] J. S. Prauzner-Bechcicki, K. Sacha, B. Eckhardt, and J. Zakrzewski, Phys. Rev. Lett. **98**, 203002 (2007).
[21] J. S. Prauzner-Bechcicki, K. Sacha, B. Eckhardt, and J. Zakrzewski, Phys. Rev. A **78**, 013419 (2008).
[22] J. H. Thiede, B. Eckhardt, D. K. Efimov, J. S. Prauzner-Bechcicki, and J. Zakrzewski, Phys. Rev. A **98**, 031401(R) (2018).
[23] J. Strohaber, A. A. Kolomenskii, and H. A. Schuessler, J. Appl. Phys. **118**, 083107 (2015).
[24] G. G. Paulus, F. Lindner, H. Walther, A. Baltuška, and F. Krausz, J. Mod. Opt. **52**, 221 (2005).
[25] The nonaveraged data were smoothed with median filter of size 10, whereas the data that have been focal-volume averaged (FVA) were smoothed with median filter of size 1 (the highly oscillatory behavior has been mostly canceled thanks to FVA averaging).
[26] W. Becker, S. P. Goreslavski, D. B. Milošević, and G. G. Paulus, J. Phys. B: At., Mol. Opt. Phys. **51**, 162002 (2018).
[27] Y. Huismans, A. Rouzee, A. Gijsbertsen, J. H. Jungmann, A. S. Smolkowska, P. S. W. M. Logman, F. Lepine, C. Cauchy, S. Zamith, T. Marchenko, J. M. Bakker, G. Berden, B. Redlich, A. F. G. van der Meer, H. G. Muller, W. Vermin, K. J. Schafer, M. Spanner, M. Y. Ivanov, O. Smirnova, D. Bauer, S. V. Popruzhenko, and M. J. J. Vrakking, Science **331**, 61 (2011).
[28] J.-W. Geng, L.-Y. Peng, M.-H. Xu, and Q. Gong, J. Phys.: Conf. Ser. **488**, 012003 (2014).
[29] T. Remetter, P. Johnsson, J. Mauritsson, K. Varjú, Y. Ni, F. Lépine, E. Gustafsson, M. Kling, J. Khan, R. López-Martens, K. J. Schafer, M. J. J. Vrakking, and A. L'Huillier, Nat. Phys. **2**, 323 (2006).
[30] K. Varjú, P. Johnsson, J. Mauritsson, T. Remetter, T. Ruchon, Y. Ni, F. Lépine, M. Kling, J. Khan, K. J. Schafer, M. J. J. Vrakking, and A. L'Huillier, J. Phys. B: At., Mol. Opt. Phys. **39**, 3983 (2006).